Biochemistry

pubs.acs.org/biochemistry Article

Noncovalent π Interactions in Mutated Aquomet-Myoglobin Proteins: A QM/MM and Local Vibrational Mode Study

Juliana J. Antonio and Elfi Kraka*

Cite This: https://doi.org/10.1021/acs.biochem.3c00192 Read Online

ACCESS | Metrics & More | Article Recommendations | Supporting Information

ABSTRACT: Protein dynamics and function is strongly connected to the energy flow taking place. Myoglobin (Mb) and its mutations are ideal systems to study the process of vibrational energy transfer (VET) at the molecular level. Anti-Stokes ultraviolet resonance Raman studies using a tryptophan (Trp) probe, introduced at different Mb positions by amino acid replacement, have suggested that the amount of VET depends on the position of the Trp probe relative to the heme group. Inspired by this experimental work, we explored the strength of noncovalent π interactions, as well as covalent interactions for both the axial and distal ligands bound to iron in aquomet-Mb with the local vibrational mode analysis (LMA), originally developed by Konkoli and Cremer. Two sets of noncovalent interactions were investigated: (1) the interaction between the water ligand and Trp rings and (2) the interaction between the Trp and the porphyrin rings of the heme group. We assessed the strength of these noncovalent interactions via a special local mode force constant. Various Trp-modified water-bound ferric Mb proteins in the ground state were studied (6 in total) using gas-phase and QM/MM calculations followed by LMA. Our results disclose that VET is indeed dependent on the position of the Trp probe relative to the heme group but also on the tautomeric nature of distal histidine. They provide new guidelines on how to assess noncovalent π interactions in proteins utilizing LMA and how to use these data to explore VET, and more generally protein dynamics and function.

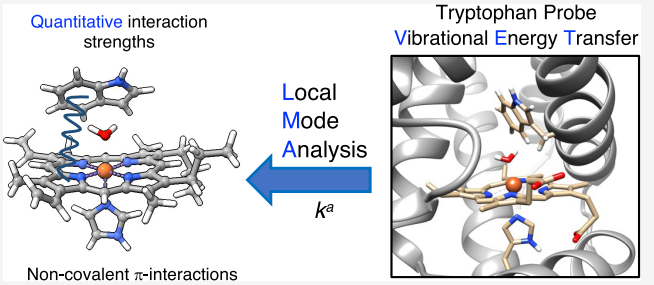

INTRODUCTION

Myoglobin (Mb), a prominent member of the globin superfamily, has an important role in a plethora of physiological functions for the heart and skeletal muscles, and as for vertebrates, it is responsible for the storage of oxygen.[1−3] Since its discovery more than 65 years ago, Mb and its mutated analogues have been studied extensively through experimental and theoretical efforts alike.[4−6] The Mb active site involves the heme porphyrin group with iron in either oxidized (ferric, Fe^{3+}) or reduced (ferrous, Fe^{2+}) form. It is fixed via Fe−N bonding with the side chain of H93 (which is commonly labeled as the proximal histidine), while the opposite portion of the heme pocket is occupied by H64 (commonly labeled as the distal histidine). Caused by this arrangement, there is only enough space for small signaling diatomic ligands such as O_2, NO, CN, and CO to enter the active site and potentially bind to iron. In the ferrous form of Mb, the diatomic ligands reversibly bind to Fe initializing different biological functions,[7−9] which has led to an increased interest in quantifying Fe−ligand bonding in these complexes.[10,11] The effect of water binding to the active site of ferric Mb (labeled as aquomet-Mb) has been another target of interest because it allows us to illuminate the dual role of the distal histidine (H64) in stabilizing ligand binding at the heme and controlling access to the protein interior.[12] Besides altering the ligand of the active site, others have modified the Mb protein to study a variety of different properties such as metal−ligand interactions (typically through resonance Raman techniques),[13] protein function,[14] and dynamics.[15]

Recently, Mb and heme-containing proteins have attracted attention for their handling of photoexcitation through vibrational energy transfer (VET).[16,17] VET studies can actually provide more detailed information about the relationship between protein dynamics and function.[18−25] Studies of the VET pathways either via experimental anti-Stokes ultraviolet resonance Raman (UVRR) spectroscopy or through molecular dynamics (MD) simulations have suggested that nonbonded atomic contacts play a significant role in the vibrational energy flow.[26−28] However, it is important to note that for the spectroscopic study of Mb proteins, mutations are necessary by adding a probe, typically tryptophan (Trp)[29] close to the active site, which can be easily identified in the spectrum. Recent studies on aquomet-Mb have revealed that upon photoexcitation of the heme group, the vibrational energy flow occurs from the heme group to the Trp probe residue, and then from

Received: April 13, 2023
Revised: June 27, 2023

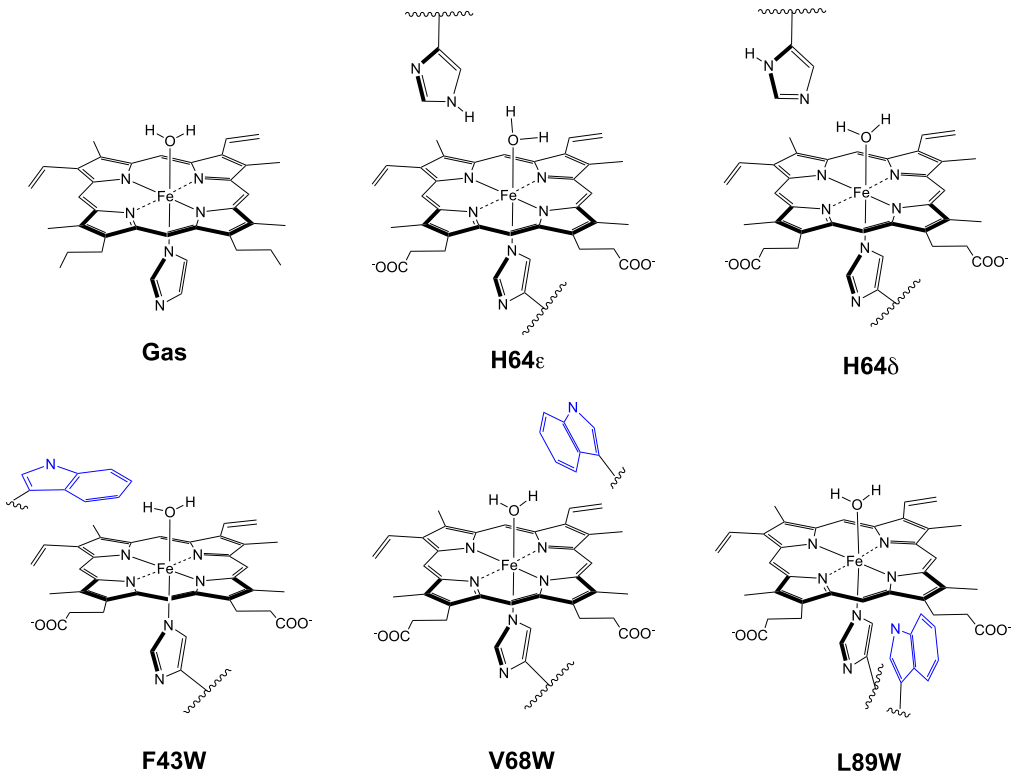

Figure 1. Aquomet-Mb active site model in the gas phase (**Gas**), QM portion of aquomet-Mb **H64***ϵ*, **H64***δ*, **F43W**, **V68W**, and **L89W**. All of the modified Trp aquomet-Mb proteins have been calculated with both **H64***ϵ* and **H64***δ* in the MM portion. For a detailed description, refer to the text. Snapshots of the active site pocket for all aquomet-Mb systems investigated in this work are collected in the Supporting Information, in Figure S1.

the Trp probe residue to the water solvent that surrounds the heme pocket.[27,29,30] With this study, they were also able to conclude that VET did not occur through the bonded atomic contacts (such as the bonding of Fe−N from the proximal histidine), but rather through noncovalent interactions that occur from the porphyrin rings of the heme group, to the 5- and 6-membered rings of Trp. Further studies showed that the positioning of the Trp probe in aquomet-Mb proteins can lead to different anti-Stokes shifts from UVRR, and postulated that the number of atomic contacts that can occur from the Trp residue to the heme is not the determining factor for the proteins' ability to have faster vibrational energy flow.[30] As such, the anti-Stokes shift intensity decreases in the order of **V68W** > **F43W** > **L89W**. In Figure 1(bottom), the snapshot of the active site of aquomet-Mb with the different Trp positions is displayed.

Inspired by the study from Mizuno and collaborators,[30] we wanted to quantify these important observations, focusing on the following objectives:

1. To derive intrinsic FeO and FeN bond strength measures based on local vibrational force constants and related bond strength orders BSO *n*.
2. To quantify for the first time the strength of the interaction between water and the Trp probe as well as between Trp and the heme group, based on a special local force constant designed for π interactions between two monomers.
3. To determine if these noncovalent π interaction strengths correlate with the associated anti-Stokes shifts as suggested by Mizuno and collaborators.[30]
4. Based on our results, to derive a general protocol for the assessment of noncovalent π interactions in proteins.

The structure of this paper is as follows: First, a brief overview of local vibrational mode theory, description of noncovalent π interactions with regard to local vibrational mode theory, the relative bond strength order, and the computational details are reported. Then, a brief discussion on the bond strengths of FeO and FeN will be presented, utilizing common quantum electronic structure methods to describe the active site environment of the modified aquomet-Mb proteins. Finally, the interaction strengths of water-Trp and Trp and the porphyrin group will be discussed, as well as the protocol/procedure used to obtain accurate descriptions of noncovalent π interactions.

THEORETICAL AND COMPUTATIONAL METHODS

Local Vibrational Mode Theory. To understand the interaction strengths between FeO, FeN, and the noncovalent π interactions such as water-Trp and Trp-porphyrin ring, LMA has been utilized in this work. The theory and application of LMA have been described and published in previous works;[31−36] therefore, only some important highlights regarding LMA will be presented. The normal mode analysis for a polyatomic molecule that is vibrating with N atoms is based on Wilson's equation of vibrational spectroscopy[37−41]

$$\mathbf{F}^{\mathbf{x}}\mathbf{L} = \mathbf{M}\mathbf{L}\boldsymbol{\Lambda} \tag{1}$$

where the force constant matrix $\mathbf{F}^{\mathbf{x}}$ is expressed in Cartesian coordinates x_i (i = 1, ⋯ 3N), and the matrix $\mathbf{L}$ collects the vibrational eigenvectors $\mathbf{l}_\mu$ as its columns (μ = 1, ⋯ N_{vib}). The diagonal mass matrix $\mathbf{M}$ comprises the atomic mass for each atom three times to account for the motion in the *x*, *y*, and *z* directions. $\boldsymbol{\Lambda}$ is a diagonal matrix with the eigenvalues $\boldsymbol{\lambda}_\mu$, which

https://doi.org/10.1021/acs.biochem.3c00192
Biochemistry XXXX, XXX, XXX−XXX

leads to the static (harmonic) vibrational frequencies ω_μ according to $\lambda_\mu = 4\pi^2c^2\omega_\mu^2$.

To work in the space of internal coordinates **q** rather than in Cartesian coordinates **x**, the Wilson equation takes a new form[37]

$$\mathbf{F}^q\mathbf{D} = \mathbf{G}^{-1}\mathbf{D}\mathbf{\Lambda} \tag{2}$$

where **D** collects the normal mode vectors $\mathbf{d}_\mu$ ($\mu = 1, \cdots N_{\text{vib}}$) column-wise, and the Wilson matrix **G**, which is defined as

$$\mathbf{G} = \mathbf{B}\mathbf{M}^{-1}\mathbf{B}^\dagger \tag{3}$$

and represents the kinetic energy in terms of internal coordinates. The elements of the rectangular matrix **B** in eq 3 are defined by the partial derivatives of internal coordinates q_n ($n = 1, 2, 3 \cdots N_{\text{vib}}$) with respect to Cartesian coordinates x_i ($i = 1, 2, 3 \cdots 3N$)

$$\mathbf{B}_n = \frac{\delta q_n(\mathbf{x})}{\delta x_i} \tag{4}$$

Whenever a new set of coordinates is introduced, the first step is to derive the appropriate **B** matrix, which is essential for the definition of intermonomer modes. This is because the **B** matrix plays a critical role in the Wilson equation of spectroscopy since it connects different sets of coordinates (symmetry, internal, curvilinear, etc.),[42−44] or Cremer−Pople ring puckering coordinates,[45] with Cartesian coordinates.[37]

Diagonalization of eq 2 leads to

$$\mathbf{D}^\dagger\mathbf{F}^q\mathbf{D} = \mathbf{K} \tag{5}$$

The transformation of the normal coordinates **Q** leads to the diagonal force constant matrix **K** collecting normal vibrational constants and matrix **D** collecting the normal mode vectors $\mathbf{d}_\mu$ in internal coordinates and is a standard procedure in modern quantum chemistry packages.[46] As such, the normal mode stretching force constant has become a popular measure of bond strength. However, normal coordinates **Q** are generally a linear combination of internal coordinates **q** or Cartesian coordinates **x**[47]

$$Q_\mu = \sum_j^{N_{vib}} (\tilde{\mathbf{D}}^\dagger G^{-1})_{\mu j} q_j \tag{6}$$

$$Q_\mu = \sum_j^{3N} (\tilde{\mathbf{D}}^\dagger G^{-1} B)_{\mu j} x_j \tag{7}$$

which indicates that normal vibrational modes are generally delocalized over the molecule, limiting the direct use of normal mode stretching force constants and normal mode frequencies as a bond strength measure. As such, local vibrational modes $\mathbf{a}_n$, local vibrational frequencies ω_n^a, and the related local force constants k_n^a are needed. Konkoli and Cremer[31−35,48,49] derived local vibrational modes $\mathbf{a}_n$ from the diagonal force constant matrix **K** and the normal mode vectors $\mathbf{d}_\mu$

$$\mathbf{a}_n = \frac{\mathbf{K}^{-1}\mathbf{d}_n^\dagger}{\mathbf{d}_n\mathbf{K}^{-1}\mathbf{d}_n^\dagger} \tag{8}$$

where the local vibrational mode $\mathbf{a}_n$ is expressed in terms of normal coordinates **Q** and $\mathbf{d}_n$ is the n-th row vector of the **D** matrix. For a comprehensive review of the derivation and discussion of LMA theory, the reader is referred to a recent review article.[35]

To each local vibrational mode $\mathbf{a}_n$, a corresponding local mode frequency ω_n^a, local mode mass m_n^a, and local force constant k_n^a, can be defined. The local mode frequency ω_n^a is defined by

$$\omega_n^a = \frac{1}{2\pi c}\sqrt{\frac{k_n^a}{m_n^a}} \tag{9}$$

and the corresponding local force constant k_n^a by

$$k_n^a = (\mathbf{d}_n\mathbf{K}^{-1}\mathbf{d}_n^\dagger)^{-1}, \quad \mathbf{d}_n = \mathbf{B}_n\mathbf{L} \tag{10}$$

Description of Noncovalent π Interactions. Recently, our group has been able to describe noncovalent π interactions with intermolecular local force constants in a dimeric system,[50,51] where there are two isolated nonlinear polyatomic monomers (A and B). As such, one can choose a set of nonredundant $N_{\text{vib}}^{\text{A}} = 3N_{\text{A}} - 6$ local modes for monomer A and another set of nonredundant $N_{\text{vib}}^{\text{B}} = 3N_{\text{B}} - 6$ local modes for monomer B. When the two monomers combine to form the complex AB, there are twelve translations and rotations, six of which are then transformed into intermolecular vibrations which describe the stretching, bending, and torsion of the monomers that are relative to each other. Therefore, the new set of nonredundant local modes for the dimer is described by $N_{\text{vib}}^{\text{AB}} = N_{\text{vib}}^{\text{A}} + N_{\text{vib}}^{\text{B}} + 6$ local modes. To define the true intermolecular vibrations between the dimers, both monomers have to be rotated into a standard orientation that is unique − something which is not generally possible. In this work, however, since there is always one monomer that is a ring, the rectangular coordinate system can be rotated into the standard orientation, uniquely defined by the Cremer−Pople mean ring plane of the ring atoms.[45]

Each atom in monomers A and B has to be rotated into the standard orientation by a 3 × 3 rotation matrix **r**.[45] Essentially the coordinate system is transformed from the initial xyz coordinates to the standard $x'y'z'$. This brings the dimer AB into the standard orientation. As shown in Figure 2, O_A is the geometric center of the rotated monomer A, and for monomer B O_B and $x'y'z'$ define the standard orientation that is determined by the mean plane, respectively, with $x''y''z''$ being the shifted coordinate system $x'y'z'$ from O_B to O_A. In this work, we have the interaction strength between water and Trp; therefore, monomer A would represent the water molecule, and monomer B represents either the 6-membered ring from Trp or the 5-membered ring from Trp. Since we are dealing with geometric

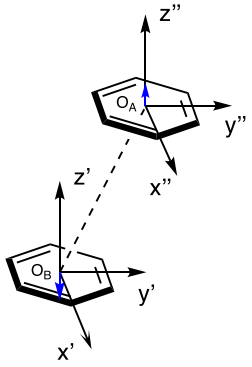

Figure 2. Definition of the S_z interaction between a benzene ring A and a benzene ring B. O_A is the geometric center of the rotated monomer A, and O_B and $x'y'z'$ define the standard orientation of ring B determined by the mean ring plane.[45] $x''y''z''$ is the shifted coordinate system $x'y'z'$ from O_B to O_A.

https://doi.org/10.1021/acs.biochem.3c00192
Biochemistry XXXX, XXX, XXX−XXX

centers of rings, we have separated the Trp into two distinct rings. The issue with treating Trp as one ring is the geometric center would be represented near the double bond where the 5-membered and 6-membered ring would meet, which does not describe the interaction that well or accurately. We also have the interaction strength between the porphyrin (which has eight different locations of 5-membered and 6-membered rings) and the Trp, which has two rings (a 6-membered ring and a 5-membered ring), with monomer A indicating either the 5- or 6-membered ring from Trp, and monomer B indicating one of the eight 5- or 6-membered porphyrin rings. Therefore, since monomers A and B are both rings, O_A and O_B, along with $x'y'z'$, define the standard orientation that is determined by the mean plane, with $x''y''z''$ being the shifted coordinate system $x'y'z'$ from O_B to O_A.

Three mass-irrelevant (where atomic mass is equal to 1) translational modes ($\mathbf{T}_B^x$, $\mathbf{T}_B^y$, $\mathbf{T}_B^z$) and three mass-irrelevant rotational modes ($\mathbf{R}_B^x$, $\mathbf{R}_B^y$, $\mathbf{R}_B^z$) in the x', y', and z' axes can be defined for monomer B(which is a ring monomer). In a similar fashion, column arrays $\mathbf{T}_A^x$, $\mathbf{T}_A^y$, $\mathbf{T}_A^z$, $\mathbf{R}_A^x$, $\mathbf{R}_A^y$, and $\mathbf{R}_A^z$ can be obtained for monomer A. When applying Wilson's **B**-matrix formulation,[37] these monomer modes define nine intermonomer modes. If the atoms in monomer A are given first, Wilson's **B**-matrices (which are row arrays) of nine intermolecular modes are given by

$$\mathbf{b}^{\dagger}(S_X) = \begin{pmatrix} \frac{1}{\sqrt{N_A}}\mathbf{T}_A^X \\ \frac{-1}{\sqrt{N_B}}\mathbf{T}_B^X \end{pmatrix}, \quad \mathbf{b}^{\dagger}(R_X) = \begin{pmatrix} \frac{1}{\sqrt{N_A}}\mathbf{R}_A^X \\ \frac{1}{\sqrt{N_B}}\mathbf{R}_B^X \end{pmatrix},$$

$$\mathbf{b}^{\dagger}(A_X) = \begin{pmatrix} \frac{1}{\sqrt{N_A}}\mathbf{R}_A^X \\ \frac{-1}{\sqrt{N_B}}\mathbf{R}_B^X \end{pmatrix} \tag{11}$$

with $X = x$, y, or z with intermolecular stretching S, rotation R, and antirotation modes A being represented and the deformation amplitude of each monomer set to one with a factor of $1/\sqrt{N_A}$ or $1/\sqrt{N_B}$, respectively. The **B**-matrices represented in eq 11 have to then be rotated back to the initial orientation by **r**. Out of the nine intermolecular modes, three intermolecular stretching modes (S_x, S_y, S_z) and three intermolecular rotational modes (R_x, R_y, R_z) are chosen to construct a set of six nonredundant intermonomer coordinates. As such, the three intermonomer stretching modes; S_x and S_y describe the sliding of monomer A along the mean plane of the ring system B in two orthogonal directions, and S_z reflects the accurate stretching between monomers A and B, and thus its interaction.

Relative Bond Strength Order. The use of relative bond strength order (BSO n) is convenient when comparing a relatively large set of k_n^a values. According to the generalized Badger rule derived by Cremer, Kraka, and co-workers, both k_n^a and BSO n are connected via the following power relationship

$$\text{BSO } n = A(k_n^a)^B \tag{12}$$

The constants A and B are determined by two reference compounds with known BSO n and k_n^a values; the requirement being for a zero-force constant, BSO n equals zero. In this work, the references used for the FeO and FeN bonds were FeH as a bond close to a single bond[52,53] and FeO as a bond close to a double bond.[54,55] Mayer bond orders[56−58] were used to quantify the single- or double-bond character, with $n(Mayer, FeH) = 0.83281$ and $n(Mayer, FeO) = 1.47459$, which corresponds to a ratio of 1.00:1.7706. Corresponding A and B constants were 0.729 and 0.537, respectively.

In this work, the covalent character of FeO and FeN bonds was determined via the Cremer−Kraka criterion[59,60] of covalent bonding which is based on the local electron density $H(r)$

$$H(\mathbf{r}) = G(\mathbf{r}) + V(\mathbf{r}) \tag{13}$$

where the kinetic energy density is $G(r)$ (positive, destabilizing) and the potential energy density is $V(\mathbf{r})$ (negative, stabilizing). Where the bond critical point $\mathbf{r}_b$ of the electron density $\rho(\mathbf{r})$ is taken between two bonded atoms, $H(\mathbf{r}_b) < 0$ indicates a covalent bond, while $H(\mathbf{r}_b) > 0$ indicates an electrostatic interaction.

Computational Details. Protein geometries were based on previous X-ray structures of modified whale sperm water-bound ferric Mb proteins (PDB: 1BZ6,[61] 2E2Y,[62] 2OH9,[63] 1CH3[64]). For consistency, all proteins started with the C-terminal of valine and ended in the N-terminal of glycine. All proteins were modified to have the distal H64 histidine in both tautomeric **H64ϵ** and **H64δ** form. Missing hydrogens of all proteins were added using the *tleap* program from AMBER and were solvated with a water hydration shell (TIP3P) of 16 Å around the iron center of the heme. MM parameters of the water-bound ferric heme were obtained from a previous publication that had a similar heme porphyrin active site system.[65] AMBER ff14SB force field was used for the remainder of the protein,[66] and the protein was neutralized with corresponding Cl^- ions and minimized for 2000 steps using AMBER.[67]

After minimization, all proteins were divided into similar QM/MM regions. The QM region for **H64ϵ** and **H64δ** includes all atoms of the heme group, the water bound to the heme, and the side chains of the distal H64 and proximal H93 histidine (98 atoms). For the Trp-modified aquomet-Mb proteins, (**F43Wϵ**, **F43Wδ**, **V68Wϵ**, **V68Wδ**, **L89Wϵ**, and **L89Wδ**), the QM region includes all atoms of the heme group, the water bound to the heme, the side chains of Trp and the proximal H93 histidine (102 atoms). The rest of the protein atoms, water molecules, and Cl^- ions were included in the MM region (average number of MM atoms, 2609).

All gas-phase calculations were performed with the ωB97X-D functional[68] and Pople's 6-31G(d,p) basis set.[69,70] QM/MM calculations were performed at the ωB97X-D/6-31G(d,p)/AMBER level of theory using the ONIOM methodology,[71] first optimizing with mechanical embedding without constraints and then with electronic embedding using scaled charges (with a value of 0.6) of MM atoms, which are close to atoms of the QM region.[67] Scaled charges prevent over-polarization of the QM electron density by MM point charges and prevent oscillations in geometry optimization. It has been suggested that the spin state of aquomet-Mb is a high spin state, indicating that there are unpaired electrons and thus has paramagnetic properties.[72] To ensure that the protein structures were in the ground state, optimizations for the doublet (S = 1/2), quartet (S = 3/2), and sextet (S = 5/2) states were performed. The energies were compared, with the quartet state being the most energetically favorable (about 15 kcal/mol more stable than the doublet and sextet state). For both the gas-phase and QM/MM calculations, full geometry optimization was performed, followed by harmonic frequency calculations, and subsequently by local mode analysis. All vibrational frequency calculations were

https://doi.org/10.1021/acs.biochem.3c00192
Biochemistry XXXX, XXX, XXX−XXX

Table 1. Calculated FeO Distances *d*, Local Mode Force Constants k^a, and Corresponding Bond Strength Orders BSO *n*, Energy Densities $H(r_b)$, as well as NBO Charges for Fe and O[a]

protein	*d* (Å)	k^a (mDyn/Å)	BSO *n*	$H(r_b)$ (Hartree/Å^3)	Fe charge (e)	O charge (e)
H64ϵ	2.337	0.349	0.488	−0.006	1.236	−0.950
H64δ	2.076	0.829	0.712	−0.006	1.388	−0.920
F43Wϵ	2.248	0.481	0.562	−0.007	1.688	−0.942
F43Wδ	2.245	0.500	0.571	−0.007	1.460	−0.940
V68Wϵ	2.707	0.043	0.196	−0.001	1.250	−0.968
V68Wδ	2.2746	0.391	0.513	−0.006	1.465	−0.947
L89Wϵ	2.365	0.290	0.450	−0.006	1.388	−0.950
L89Wδ	2.283	0.390	0.512	−0.006	1.464	−0.943
Gas	2.006	1.113	0.810	−0.005	1.220	−0.890

[a]Gas-phase calculations at the ωB97X-D/6-31G(d,p) level of theory and QM/MM calculations at the ωB97X-D/6-31G(d,p)/AMBER level of theory.

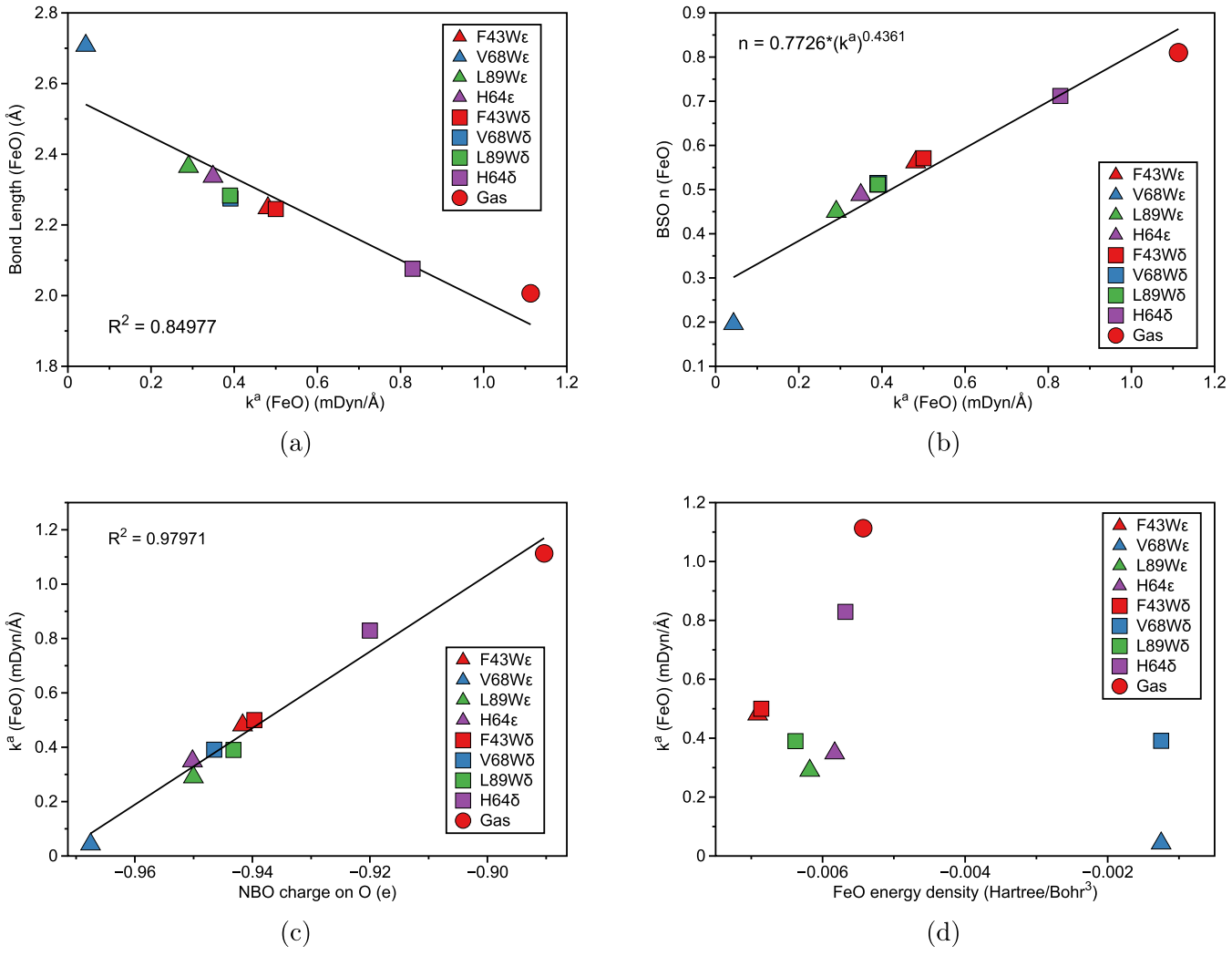

Figure 3. Plots of (a) FeO bond length (Å) versus local force constant k^a (mDyn/Å), (b) bond strength order BSO *n* for FeO bonds calculated from local force constants k^a(FeO) via eq 12, (c) FeO local force constant k^a versus NBO charge of the O atom of FeO and (d) FeO local force constant k^a versus energy density (Hartree/Bohr^3) for the systems investigated. Gas-phase calculations at the ωB97X-D/6-31G(d,p) level of theory and QM/MM calculations at the ωB97X-D/6-31G(d,p)/AMBER level of theory.

completed with no imaginary frequencies, indicating that all structures are at a minima on the potential energy surface. All DFT calculations were carried out on Gaussian16.[46] The local mode analysis was performed with LMODEA.[73] Natural Bond Orbital (NBO) charges were calculated with the NBO program.[74,75] Energy densities at bond critical points were calculated using the AIMALL program.[76]

https://doi.org/10.1021/acs.biochem.3c00192
Biochemistry XXXX, XXX, XXX−XXX

Table 2. Calculated FeN Distances *d*, Local Mode Force Constants k^a, and the Corresponding Bond Strength Orders BSO *n*, Energy Densities $H(r_b)$, as well as NBO Charges for Fe and N[a]

protein	*d* (Å)	k^a (mDyn/Å)	BSO *n*	$H(r_b)$ (Hartree/Å^3)	Fe charge (e)	N charge (e)
H64ϵ	2.057	1.411	0.898	−0.013	1.236	−0.646
H64δ	2.132	1.009	0.776	−0.014	1.388	−0.575
F43Wϵ	2.067	1.378	0.889	−0.019	1.688	−0.659
F43Wδ	2.060	1.429	0.903	−0.015	1.460	−0.552
V68Wϵ	2.038	1.544	0.935	−0.013	1.250	−0.644
V68Wδ	2.075	1.326	0.874	−0.014	1.465	−0.601
L89Wϵ	2.034	1.594	0.948	−0.014	1.388	−0.641
L89Wδ	2.059	1.435	0.905	−0.014	1.464	−0.612
Gas	1.9277	2.109	1.071	−0.025	1.220	−0.513

[a]Gas-phase calculations at the ωB97X-D/6-31G(d,p) level of theory and QM/MM calculations at the ωB97X-D/6-31G(d,p)/AMBER level of theory.

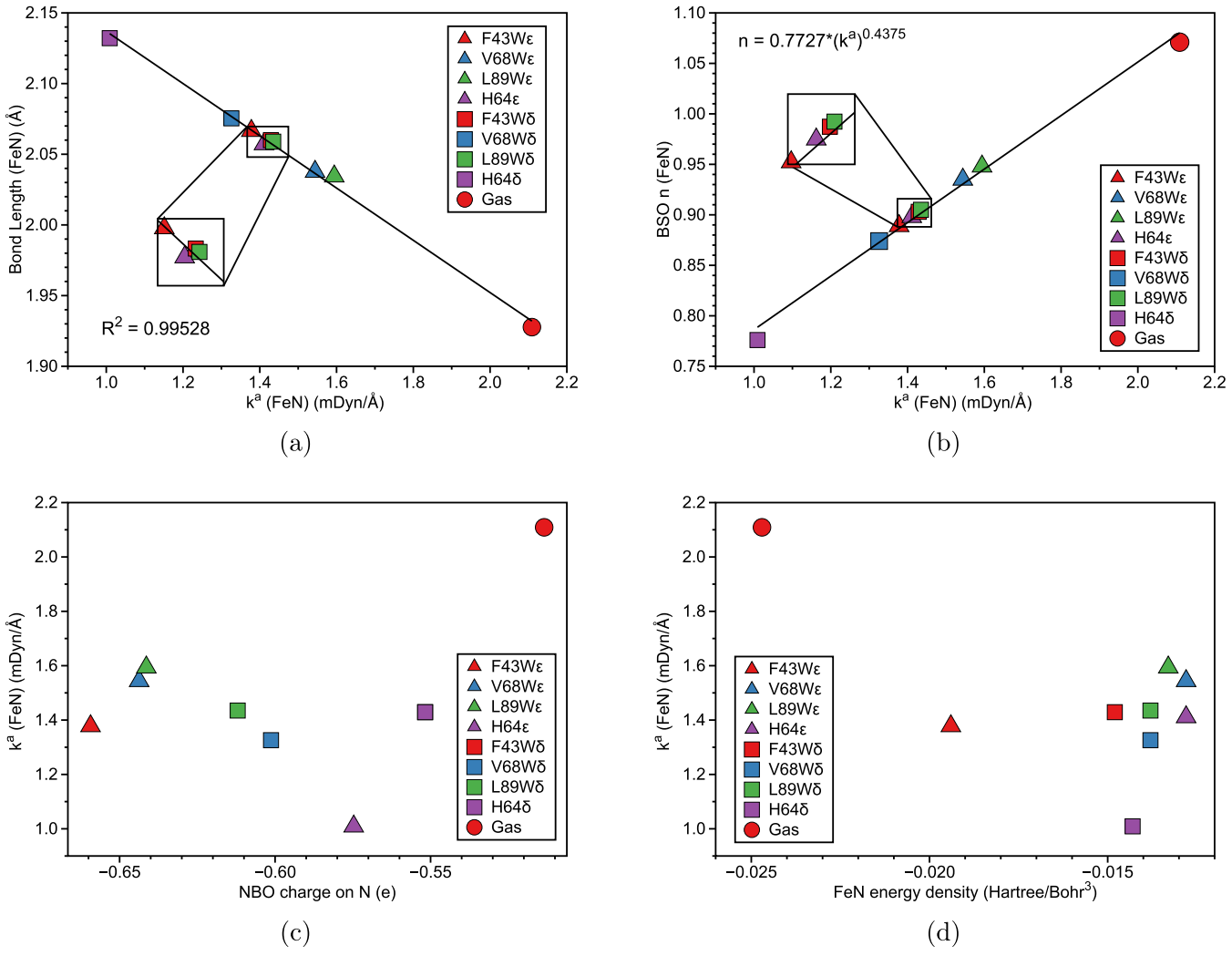

Figure 4. Plots of (a) FeN bond length (Å) versus local force constant k^a(FeN) (mDyn/Å), (b) bond strength order BSO *n* for FeN bonds calculated from local force constants k^a(FeN) via eq 12, (c) FeN local force constant k^a vs NBO charge of the N atom of FeNb and (d) FeN local force constant k^a vs FeN energy density (Hartree/Bohr^3) for the systems investigated. Gas-phase calculations at the ωB97X-D/6-31G(d,p) level of theory and QM/MM calculations at the ωB97X-D/6-31G(d,p)/AMBER level of theory.

RESULTS AND DISCUSSION

Utilizing the computational approach of combining QM/MM with LMA, we were able to elucidate 9 different aquomet-Mb systems at the ground state; the aquomet active site model in the gas phase (**Gas**), the aquomet-Mb ϵ and δ tautomers (see Figure 1), as well as the 6 aquomet-Mb protein mutations involving the replacement of a variety of amino acids that are near the active site with Trp. In the following sections, the results of FeO, FeN, water-Trp, and Trp-porphyrin interactions will be discussed.

https://doi.org/10.1021/acs.biochem.3c00192
Biochemistry XXXX, XXX, XXX−XXX

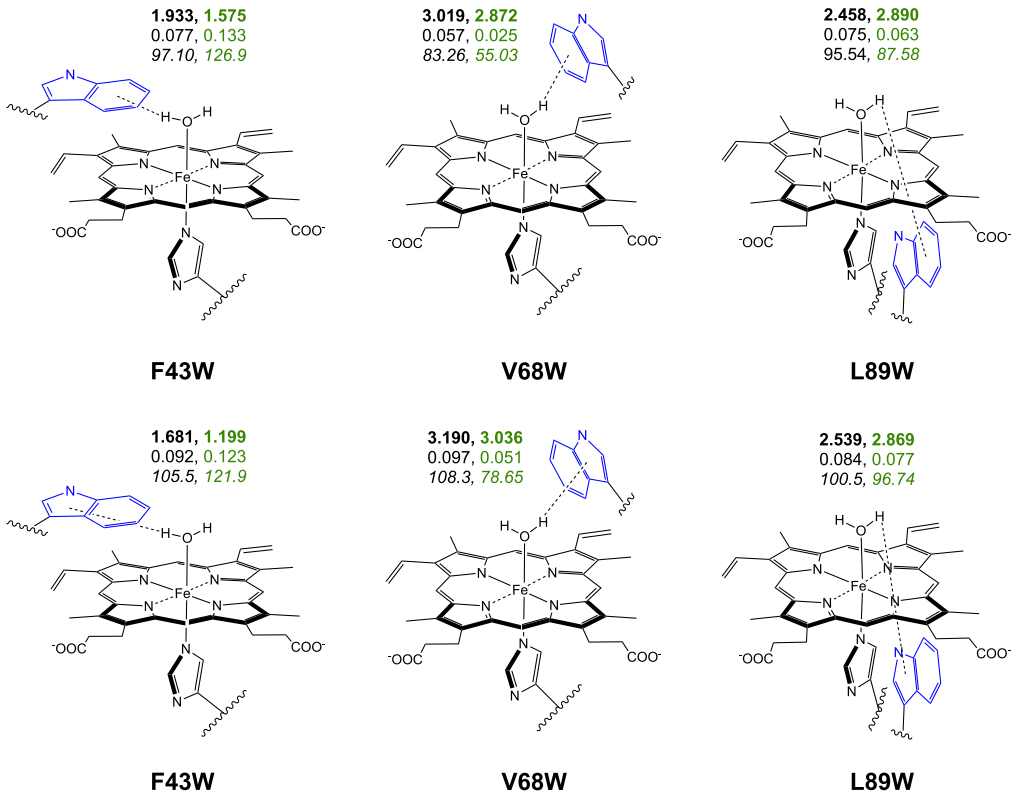

Figure 5. Noncovalent π interaction strengths between Trp and water in various mutated proteins. The black font represents the **H64**ϵ protein, whereas the green font represents the **H64**δ protein. Bold font represents the local bond distance (Å), regular font represents the local force constant (mDyn/Å) and italicized font represents the local stretching frequency (cm^{-1}).

FeO and FeN Bond Strength. In Table 1, the calculated FeO bond distances d, local mode force constants k^a, and corresponding bond strength orders BSO n, energy densities $H(\mathbf{r}_b)$, as well as NBO charges for Fe and O for the wild-type and mutated aquomet-Mb proteins are shown that were investigated in this work. In Figure 3a,b, correlations between the local force constant, bond length, and bond strength order are illustrated. In Figure 3a, local force constants k^a(FeO) are compared with the FeO distances (Å), in which we find a correlation (albeit some scattering occurring with an R^2 value of 0.84977) between the bond length of FeO (in Å) and the local force constant k^a (in mDyn/Å).

For the systems that were studied in this work, it appears that the general trend is the stronger FeO bonds have the corresponding shorter bond length (i.e., **Gas** d = 2.006 Å and **H64**δ d = 2.337 Å), whereas the weakest bond is always the longest (**V68W**ϵ d = 2.707 Å). This bond strength relationship is further confirmed in Figure 3b, where the BSO n values for the FeO bonds are calculated with the power relationship as described by the generalized Badger rule of Kraka, Larsson, and Cremer.[77] The generalized Badger rule predicts an inverse power relationship between the bond length and the local force constant for diatomic molecules to polyatomic compounds by replacing normal mode force constants with their local mode counterparts, extending Badger's original rule.[78] However, it is not always true that the stronger bond is the shorter bond, as realized in our group's previous publications.[79,80] For our investigated systems, with very minimal changes in the FeO bond length due to the nature of the Mb pocket space confinement, the generalized Badger rule is valid.[10,11] Figure 3c shows the relation between FeO local force constant and the NBO atomic charge on the O atom of FeO. According to Figure 3c, the strongest FeO bonds (**Gas** and **H64**δ) have the less negative NBO atomic oxygen charge (−0.890 e and −0.920 e, respectively), whereas the weakest FeO bond (**V68W**ϵ) has the most negative oxygen charge (−0.968 e). Figure 3d further supports the general trend for the FeO bonds that the stronger FeO bond has a slightly more covalent character as reflected by the $H(\mathbf{r}_b)$ values that are shown in Figure 3d.

In Table 2, the calculated FeN distances, local mode force constants, and corresponding bond strength orders BSO n, energy densities, as well as NBO charges for Fe and N are shown. Figure 4a displays the relationship between the FeN distances and the local force constants k^a(FeN), with a great correlation (R^2 = 0.99528) between them. The same trend that is seen in the FeO bond lengths with respect to the local force constants is also applicable to the FeN distances. However, it is important to distinguish that there is no inverse relationship of local force constants that occurs between FeO and FeN. This is realized with the shortest and strongest FeN bonds being the **Gas** molecule (d = 1.928 Å) and one of the mutated Trp proteins, **L89W**δ (d = 2.059 Å). **Gas** has both the strongest and shortest bonds for FeO and FeN. It is interesting to note that **Gas** also has the lowest NBO charges for Fe (1.220 e), O (−0.890 e), and N (−0.513 e) compared to the wild-type and mutated aquomet-Mb proteins. The longest and weakest FeN bonds are **H64**δ (d = 2.132 Å) and **V68W**δ (d = 2.075 Å).

Although it was previously mentioned that there is no apparent inverse relationship between the FeO and FeN when it comes to bond strength, the **H64**δ FeO bond is the second strongest after **Gas**, however with the FeN bond, it is the weakest. This relationship between bond length and local force

https://doi.org/10.1021/acs.biochem.3c00192
Biochemistry XXXX, XXX, XXX−XXX

constant is further expanded in Figure 4b, where it clearly confirms that the longer bond is indeed weaker than its shorter and stronger bond counterpart. Figure 4c displays the relationship between NBO atomic charge on the N atom and the corresponding FeN local force constant. Albeit a weak correlation, the NBO atomic charge on the N atom for the **Gas** molecule again has the lowest charge (−0.513 e) and strongest FeN local force constant. Since the **Gas** phase molecule is only the porphyrin with the water bound to Fe, it does not deal with the amount of constraint in the Mb pocket that the rest of the mutated aquomet-Mb proteins do. In Figure 4d, the energy density and local force constant is compared, where it is revealed that the energy density for the FeN bond keeps a similar trend with the more covalent character having a higher local force constant (with some scattering due to the nature of the proximal histidine and the compactness of the aquomet-Mb pocket).

Bond Strength of Water and Trp. The first noncovalent interaction that was calculated was the water that is bound to the iron porphyrin ring and the Trp at various places within the Mb protein. As shown in Figure 5, there are two different interactions that can occur within each protein, one with the 5-membered ring and the other with the 6-membered ring. Altogether, the six mutated proteins yield about 12 different interaction strengths. For Figure 5, the black font represents the **H64**ϵ protein, whereas the green font represents the **H64**δ protein. Also, the local bond distance (in bold font, Å), local force constant (in regular font, mDyn/Å), and the local stretching frequency (in italicized font, cm^{-1}) are shown in the figure. For Figure 5 (top), the interaction between water (3 atoms) and the 6-membered ring of Trp (6 atoms) are shown for the different mutated aquomet-Mb proteins (**F43W**ϵ, **F43W**δ, **V68W**ϵ, **V68W**δ, **L89W**ϵ, and **L89W**δ). The general trend for the bond distance of the interaction between water and the 6-membered Trp ring is **F43W**δ and **F43W**ϵ has the shortest bond distance (d = 1.575 Å and d = 1.933 Å, respectively) and the strongest local force constant (0.133 mDyn/Å and 0.077 mDyn/Å, respectively). This is followed by **L89W**ϵ (d = 2.458 Å, 0.075 mDyn/Å) and **L89W**δ (d = 2.890 Å, 0.063 mDyn/Å), with the weakest interactions for the aquomet-Mb proteins being **V68W**ϵ (d = 3.019 Å, 0.057 mDyn/Å) and **V68W**δ (d = 2.872 Å, 0.025 mDyn/Å). It is interesting to note that the lowest local force constant from **V68W**δ does not follow the general trend of the longer bond being the weaker bond. If it were following this trend, it would actually be the third weakest interaction strength. However, this is not the case and is most likely due to the hydrogen bonding that is occurring between the hydrogen of the water and the nitrogen of the distal histidine. It is also worth mentioning that in the **L89W** protein(s) (in both H64 tautomeric forms), the water-Trp interaction has a porphyrin ring between the bound water and the Trp. Therefore, in the calculations of the noncovalent π interaction strengths between them, there are the porphyrin π electrons that are geometrically obstructing the interaction strength, which can affect the interaction between the geometric center-point between monomer B and monomer A. This is not observed for the **F43W** and **V68W** proteins, only for the **L89W** proteins. With the **F43W**δ protein, the position and proximity of the Trp do not allow for the hydrogen of the water to be a hydrogen-bond donor to the distal histidine portion. Also, it is interesting to note that the frequency generally decreases as the local force constant decreases.

In Figure 5(bottom), the interaction between water and the 5-membered ring of Trp is shown for the mutated aquomet-Mb proteins. Different from the interaction between water and the 6-membered Trp ring, the strongest local force constants are from **F43W**δ and **V68W**ϵ (0.123 mDyn/Å and 0.097 mDyn/Å, respectively). However, the bond distance for the interaction of **V68W**ϵ is not the shortest (d = 3.190 Å), with the distance actually being the longest out of all of the other proteins with the 5-membered Trp ring interaction. This is followed by **F43W**ϵ (d = 1.681 Å, 0.092 mDyn/Å), **L89W**ϵ (d = 2.539 Å, 0.084 mDyn/Å), **L89W**δ (d = 2.869 Å, 0.077 mDyn/Å), and finally the weakest interaction strength is the **V68W**δ (d = 3.036 Å, 0.051 mDyn/Å) protein. Again, just as was seen for the 6-membered Trp ring interaction strengths and local stretching frequencies, we see a similar trend with the 5-membered Trp ring interaction strengths with the local stretching frequencies generally decreasing as the local force constant decreases.

Bond Strength of Trp-Porphyrin. To describe the interaction strength between Trp and the porphyrin ring in a coherent and comprehensive manner, it is important to distinguish where and how many interactions can occur within these two ring-containing monomers. In Figure 6, we see the depiction of such interactions that can occur with monomer A and monomer B; monomer A shows two different geometric centers, one with the 6-membered ring (**I**) and the other with the 5-membered ring (**II**), and monomer B shows eight different geometric centers in the porphyrin (**1**−**8**). As such, there are 16 different interactions that can occur in total for each protein. Altogether there are 96 interaction strengths of Trp-porphyrin for the six mutated proteins, which are defined from the S_z intermonomer stretching mode. Figures 7 and 8 display the interaction strengths between Trp and porphyrin for the six mutated proteins. In these figures, the top portion shows the interaction strengths for monomer A ring **I** and monomer B ring **1** and ring **5**, respectively, while the bottom portion shows the interaction strengths for monomer A ring **II** and monomer B either ring **1** and ring **5**, respectively. For the other six monomer B interaction strengths, the reader is referred to Figures S2a−c and S3a-c in the Supporting Information.

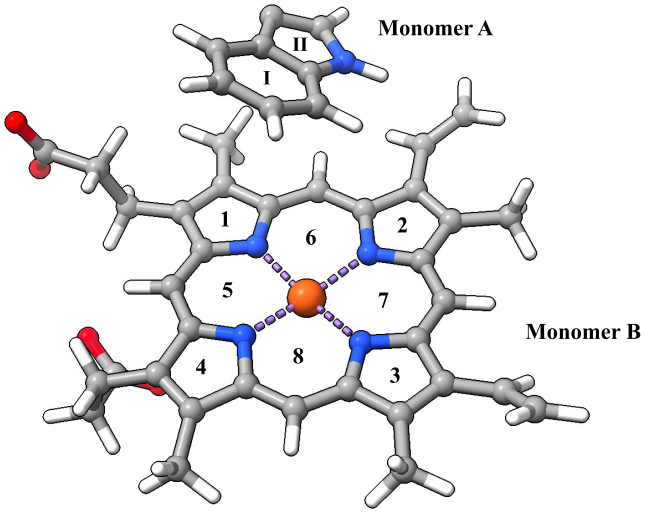

Figure 6. General snapshot of the numbering used for LMA of monomer A (Trp residue) and monomer B (porphyrin). For monomer A, ring **I** is the 6-membered ring of Trp and ring **II** is the 5-membered ring of Trp. For monomer B, rings **1**−**4** are the 5-membered rings of porphyrin, and rings **5**−**8** are the 6-membered rings of porphyrin.

https://doi.org/10.1021/acs.biochem.3c00192
Biochemistry XXXX, XXX, XXX−XXX

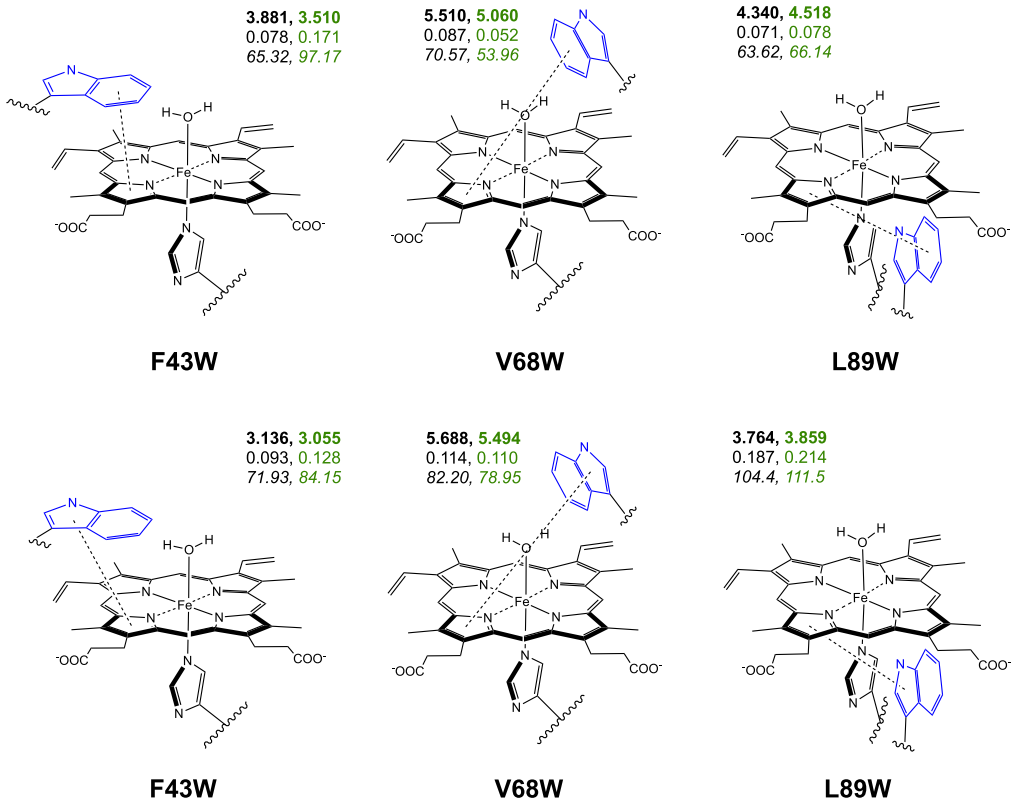

Figure 7. Nonovalent π interaction strengths between Trp and porphyrin in the various Trp-modified Mb proteins. All of the monomer B interactions are with ring **1**. The top half of the figure is with monomer A as ring **I**, whereas the bottom half is with monomer A as ring **II**. The black font represents the **H64**ϵ protein, whereas the green font represents the **H64**δ protein. Bold font represents the local bond length (Å), regular font represents the local force constant (mDyn/Å), and italicized font represents the local stretching frequency (cm^{-1}).

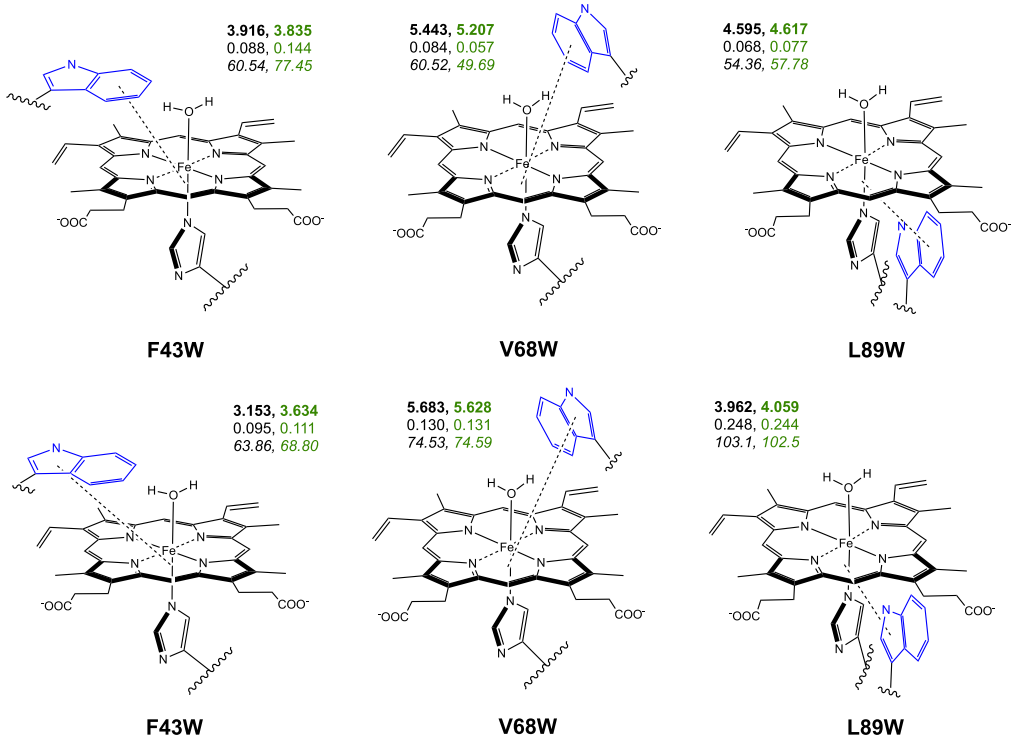

Figure 8. Noncovalent π interaction strengths between Trp and porphyrin in the various Trp-modified Mb proteins. All of the monomer B interactions are with ring **5**. The top half of the figure is with monomer A as ring **I**, whereas the bottom half is with monomer A as ring **II**. The black font represents the **H64**ϵ protein, whereas the green font represents the **H64**δ protein. Bold font represents the local bond length (Å), regular font represents the local force constant (mDyn/Å), and italicized font represents the local stretching frequency (cm^{-1}).

https://doi.org/10.1021/acs.biochem.3c00192
Biochemistry XXXX, XXX, XXX−XXX

As mentioned in the methodology section, these interaction strengths were measured with the S_z intermonomer stretching mode, as it reflects the accurate stretching between the two monomers. However, we also did a comparison of calculating the local force constant with different parameters, such as the distance between geometric centers, the distance between monomer A and (quasi-)planar monomer B, intermonomer stretching mode S_x, and intermonomer stretching mode S_y. The respective data, as well as an explanation of the difference between these parameters, can be found in the Supporting Information (Tables S1−S8). It is imperative to discuss that the local force constant, the distance between the two monomers, and the local frequency will change depending on what parameters are used to describe the interaction strength of the two monomers. This is why it is always best practice to correctly define the monomers interaction strength and the axis to which it corresponds.[51] For example, in Table S1, defining the parameter as the distance between monomer A and (quasi-)planar monomer B, the local force constants are the same as the S_z parameter, however, the distance and local frequency are different. Also, despite the porphyrin ring being highly symmetric, the eight different positions that could be used for monomer B yield eight different and varying interaction strengths and their respective trends, depending on whether it is interacting with ring **I** or ring **II** from monomer A. As such, we will be discussing the general trends that are shown from these 96 interaction strengths, grouped together and separated by the eight rings from monomer B. As previously mentioned, Figures 7 and 8 are shown for monomer B rings **1** and **5**, respectively, with the rest shown in the Supporting Information (Figure S2a-c and Figure S3a-c).

The local force constant, local bond distance, and local frequencies between the 6-membered ring (**I**) from Trp and the porphyrin ring (**1**), as well as the 5-membered ring (**II**) from Trp and the porphyrin ring (**1**) are shown in Figure 7. For the interaction between **I** and **1** on the top half of the figure, the greatest interaction strength experienced is the **F43W**δ (0.171 mDyn/Å), which has the shortest bond (d = 3.510 Å). As shown in Figures S2a-c, S3a-c, and 8, this trend of **F43W**δ having the strongest interaction and shorter local bond distance for the 6-membered ring regardless of where monomer B is placed, holds true. The second strongest interaction in Figure 7, however, is shown to be **V68W**ϵ (0.087 mDyn/Å), which is not the second shortest bond and is actually the longest bond distance (d = 5.060 Å). This does not follow the general trend shown in Figures 8, S2a, S2c, S3a, and S3c, where the usual second strongest interaction results in **F43W**ϵ (with the exception of ring **3**, Figure S2b and ring **7**, Figure S3b, which has **L89W**δ as the second strongest interaction). The lowest local force constant, which indicates the weakest noncovalent π interaction and longest local bond distance is **V68W**δ (0.052 mDyn/Å, d = 5.060 Å), and this trend holds true for the other monomer B rings (albeit ring **4** Figure S2c). In general, the trend that is seen for the 6-membered Trp rings and the 6-membered porphyrin rings, when averaging the stretching force constants of the tautomeric forms shows in order of decreasing interaction strengths to be **F43W** > **L89W** > **V68W**. The 6-membered ring of Trp and the 5-membered rings of porphyrin have a similar trend, albeit for rings **3** and **4** from the porphyrin. For the interaction strength of the 5-membered rings of Trp, the general trend for the strongest interaction strength is typically **L89W**δ, with the exception of rings **5** (Figure S2c) and **8** (Figure S3c) which has **L89W**ϵ as the strongest interaction. The general trend for the weakest interaction strength is typically **F43W**ϵ, with the exception of rings **2** (Figure S2a) and **6** (Figure S3a), which has **V68W**ϵ as the weakest interaction, and ring **4** (Figure S2c), which as **F43W**δ as the weakest interaction. Overall, when averaging the tautomeric forms, the order of decreasing interaction strengths is **L89W** > **V68W** > **F43W**, except for rings **2** and **6**, which have the order of **L89W** > **F43W** > **V68W**.

CONCLUSIONS

In this study, we have calculated the bond properties of FeO and FeN, as well as noncovalent π interactions (water-Trp and Trp-porphyrin) for the active site in aquomet-Mb proteins utilizing QM/MM calculations of optimal geometries and molecular frequencies of wild-type aquomet-Mb, including a gas-phase model, and six mutated proteins where some amino acids close to the active site were replaced with Trp. These bond properties, after QM/MM calculations, were then further studied with LMA, QTAIM method, and NBO analysis. We found that there is no inverse relationship between FeO bond and FeN bond; however, for **H64**δ, it had a stronger FeO bond and the weakest FeN bond compared to the other proteins.

The main focus of this study was to quantify the interaction strengths of the noncovalent π interactions that occur in the six mutated aquomet-Mb proteins. For this, we utilized a special parameter that defines the intermonomer stretching mode between two geometric centers of monomers A and B, with monomer B set as the standard orientation of the Cremer−Pople mean ring plane. We first calculated the water-Trp interaction strengths, with the 5-membered and 6-membered rings experiencing similar trends; **F43W**δ having the strongest interaction strength due to its proximity to the water ligand and **V68W**δ having the weakest interaction strength due to the lack of proximity and orientation with respect to the water ligand. On the other hand, the Trp-porphyrin trends that are defined by both monomer A (**I** and **II**) and monomer B (**1**−**8**) can be vastly different, and therefore it is extremely important to correctly define the parameters. In this situation, the S_z stretching force constant offers the most accurate description, with the 6-membered ring(s) of Trp having a general trend of **F43W**δ having the strongest interaction, followed by either **F43W**ϵ or **V68W**ϵ, depending on the definition of the porphyrin ring, and then followed by **L89W**δ and **L89W**ϵ. The weakest interaction appears to be **V68W**δ for the 6-membered ring on Trp. For 5-membered ring(s) of Trp the trend is different, with **L89W**δ and **L89W**ϵ having the strongest interaction strength and the weakest interaction strength is either **F43W**ϵ or **V68W**ϵ, depending on the definition of the ring in the porphyrin group. It is important to note that the difference of the results obtained by the 6-membered and 5-membered rings is due to the definition of the geometric center-point of the ring and the definition of Cremer's mean ring plane that is defined by the ring monomer B (in this situation, it was defined by the porphyrin ring). The trend of anti-Stokes shift intensities that Kondoh et. al have measured are in the order of **V68W** > **F43W** > **L89W**.[26] However, they have mentioned that the more atomic contacts between the porphyrin heme group and the Trp residue do not necessarily mean a greater anti-Stokes shift intensity. With regard to the atomic contacts between the porphyrin heme group and the Trp residue, they found the order to be **F43W** > **L89W** > **V68W**. Our results are consistent with what was found previously by Kondoh et. al, particularly the trend between the atomic contacts of the heme and Trp and our S_z stretching force constant with the 6-membered ring of Trp and the 6-membered

https://doi.org/10.1021/acs.biochem.3c00192
Biochemistry XXXX, XXX, XXX−XXX

rings of porphyrin. Therefore, we propose that our local force constants for these nonbonded, noncovalent π interactions between Trp and the porphyrin heme group at the ground state of these aquomet-Mb proteins show that the VET is dependent on the position of the Trp probe relative to the heme group, as well as the nature of the protein. The tautomeric nature of the distal histidine (whether ϵ or δ) can completely change the nature of hydrogen bonding that can occur with the water ligand in these aquomet-Mb proteins. Our studies show that the trend that is seen in VET experimental/MD studies is shown as an averaged combination of the distal histidine ϵ and δ form of the proteins. If one is interested in utilizing LMA to describe noncovalent π interactions, particularly in protein systems, correctly defining the monomers and the parameters used to describe the local stretching force constant must be taken into consideration. Nonbonded interactions are extremely important for a variety of biological processes,[81] particularly in proteins, and this work, for the first time, offers quantitative results to describe these noncovalent π interactions.

Our comprehensive results provide new guidelines on how to assess noncovalent π interactions in proteins utilizing LMA and how to use these data to explore VET, and more generally protein dynamics and function. We hope that our findings will inspire our colleagues in the biochemistry community to apply LMA also to other noncovalent π-interactions found in biochemical systems, enriching in this way our understanding of these important interactions and their role in biochemistry.

■ ASSOCIATED CONTENT

Supporting Information

The Supporting Information is available free of charge at https://pubs.acs.org/doi/10.1021/acs.biochem.3c00192.

Snapshots of the selected residues (Figure S1); noncovalent π interaction strengths (Figures S2 and S3); and calculated local distances, local force constants, and frequencies (Tables S1−S8) (PDF)

■ AUTHOR INFORMATION

Corresponding Author

Elfi Kraka − *Computational and Theoretical Chemistry Group (CATCO), Department of Chemistry, Southern Methodist University, Dallas, Texas 75275-0314, United States;* orcid.org/0000-0002-9658-5626; Email: ekraka@gmail.com

Author

Juliana J. Antonio − *Computational and Theoretical Chemistry Group (CATCO), Department of Chemistry, Southern Methodist University, Dallas, Texas 75275-0314, United States;* orcid.org/0000-0002-0358-9274

Complete contact information is available at: https://pubs.acs.org/10.1021/acs.biochem.3c00192

Notes

The authors declare no competing financial interest.

■ ACKNOWLEDGMENTS

This work was financially supported by the National Science Foundation (Grant CHE 2102461). The authors thank SMU's Center for Scientific Computing for providing generous computational resources.

■ REFERENCES

(1) Ordway, G. A.; Garry, D. J. Myoglobin: an essential hemoprotein in striated muscle. *J. Exp. Biol.* **2004**, *207*, 3441−3446.

(2) Kendrew, J. C.; Dickerson, R. E.; Strandberg, B. E.; Hart, R. G.; Davies, D. R.; Phillips, D. C.; Shore, V. C. Structure of Myoglobin: A Three-Dimensional Fourier Synthesis at 2 Å. Resolution. *Nature* **1960**, *185*, 422−427.

(3) Elkholi, I. E.; Elsherbiny, M.; Emara, M. Myoglobin: From physiological roles to potential implications in cancer. *Biochim. Biophys. Acta, Rev. Cancer* **2022**, *1877*, No. 188706.

(4) Lima, F. A.; Penfold, T. J.; van der Veen, R. M.; Reinhard, M.; Abela, R.; Tavernelli, I.; Rothlisberger, U.; Benfatto, M.; Milne, C. J.; Chergui, M. Probing the electronic and geometric structure of ferric and ferrous myoglobins in physiological solutions by Fe K-edge absorption spectroscopy. *Phys. Chem. Chem. Phys.* **2014**, *16*, 1617−1631.

(5) Falahati, K.; Tamura, H.; Burghardt, I.; Huix-Rotllant, M. Ultrafast carbon monoxide photolysis and heme spin-crossover in myoglobin via nonadiabatic quantum dynamics. *Nat. Commun.* **2018**, *9*, No. 4502.

(6) Ren, H. C.; Ji, L.; Chen, T.; Yuan, J.; Huang, Y.; DQ, W.; Ji, G.; Zhang, Z. Quasi-Static Two-Dimensional Infrared Spectra of the Carboxyhemoglobin Subsystem under Electric Fields: A Theoretical Study. *J. Phys. Chem. B* **2020**, *124*, 9570−9678.

(7) Alvarez, L.; Suarez Vega, V.; McGinity, C.; Khodade, V. S.; Toscano, J. P.; Nagy, P.; Lin, J.; Works, C.; Fukuto, J. M. The reactions of hydropersulfides (RSSH) with myoglobin. *Arch. Biochem. Biophys.* **2020**, *687*, No. 108391.

(8) Bostelaar, T.; Vitvitsky, V.; Kumutima, J.; Lewis, B. E.; Yadav, P. K.; Brunold, T. C.; Filipovic, M.; Lehnert, N.; Stemmler, T. L.; Banerjee, R. Hydrogen Sulfide Oxidation by Myoglobin. *J. Am. Chem. Soc.* **2016**, *138*, 8476−8488.

(9) Tse, W.; Whitmore, N.; Cheesman, M.; Watmough, N. Influence of the heme distal pocket on nitrile binding orientation and reactivity in Sperm Whale myoglobin. *Biochem. J.* **2021**, *478*, 927−942.

(10) Freindorf, M.; Delgado, A. A. A.; Kraka, E. CO Bonding in Hexa− and Pentacoordinate Carboxy-Neuroglobin − A QM/MM and Local Vibrational Mode Study. *J. Comp. Chem.* **2022**, *43*, 1725−1746.

(11) Freindorf, M.; Kraka, E. Critical Assessment of the FeC and CO Bond strength in Carboxymyoglobin - A QM/MM Local Vibrational Mode Study. *J. Mol. Model.* **2020**, *26*, 281−281.

(12) Cao, W.; Christian, J.; Champion, P.; Rosca, F.; Sage, J. Water Penetration and Binding to Ferric Myoglobin. *Biochemistry* **2001**, *40*, 5728−5737.

(13) Olson, J. S.; Phillips, G., Jr. Myoglobin discriminates between O_2, NO, and CO by electrostatic interactions with the bound ligand. *J. Biol. Inorg. Chem.* **1997**, *2*, 544−552.

(14) Brantley, R.; Smerdon, S.; Wilkinson, A.; Singleton, E.; Olson, J. The Mechanism of Autooxidation of Myoglobin. *J. Biol. Chem.* **1992**, *258*, 6995−7010.

(15) Kondo, H. X.; Takano, Y. Analysis of Fluctuation in the Heme-Binding Pocket and Heme Distortion in Hemoglobin and Myoglobin. *Life* **2022**, *12*, 210.

(16) Reid, K. M.; Yamato, T.; Leitner, D. Variation of Energy Transfer Rates across Protein-Water Contacts with Equilibrium Structural Fluctuations of a Homodimeric Hemoglobin. *J. Phys. Chem. B* **2020**, *124*, 1148−1159.

(17) Yamashita, S.; Mizuno, M.; Takemura, K.; Kitao, A.; Mizutani, Y. Dependence of Vibrational Energy Transfer on Distance in a Four-Helix Bundle Protein: Equidistant Increments with the Periodicity of α Helices. *J. Phys. Chem. B* **2022**, *126*, 3283−3290.

(18) Flynn, G. W.; Parmenter, C. S.; Wodtke, A. M. Vibrational Energy Transfer. *J. Phys. Chem. A* **1996**, *100*, 12817−12838.

(19) Leitner, D. M.; Pandey, H.; Reid, K. Energy Transport across Interfaces in Biomolecular systems. *J. Phys. Chem. B* **2019**, *123*, 9507−9524.

(20) Fujii, N.; Mizuno, M.; Ishikawa, H.; Mizutani, Y. Observing Vibrational Energy Flow in a Protein with the Spatial Resolution of a Single Amino Acid Residue. *J. Phys. Chem. Lett.* **2014**, *5*, 3269−3273.

(21) Baumann, T.; Hauf, M.; Schildhauer, F.; Eberl, K.; Durkin, P.; Deniz, E.; Löffler, J.; Acevdeo-Rocha, C.; Jaric, J.; Martins, B.; et al. Site-

Resolved Observation of Vibrational Energy Transfer Using a Genetically Encoded Ultrafast Heater. *Anger. Chem. Int. Ed.* **2019**, *58*, 2899−2903.
(22) Reid, K. M.; Yamato, T.; Leitner, D. Scaling of Rates of Vibrational Energy Transfer in Proteins with Equilibrium Dynamics and Entropy. *J. Phys. Chem. B* **2018**, *122*, 9331−9339.
(23) Deniz, E.; Valiño-Borau, L.; Löffler, J. G.; Eberl, K. B.; Gulzar, A.; Wolf, S.; Durkin, P. M.; Kaml, R.; Budisa, N.; Stock, G.; Bredenbeck, J. Through bonds or contacts? Mapping protein vibrational energy transfer using non-canonical amino acids. *Nat. Commun.* **2021**, *12*, No. 3284.
(24) Löffler, J. G.; Deniz, E.; Feid, C.; Franz, V. G.; Bredenbeck, J. Versatile Vibrational Energy Sensors for Proteins. *Angew. Chem., Int. Ed.* **2022**, *61*, No. e202200648.
(25) Wu, S. Energy Flow Perspective on the Mechanism of the Conformational Dynamics in Biomolecules. Ph.D. Thesis, 2022.
(26) Kondoh, M.; Mizuno, M.; Mizutani, Y. Importance of Atomic Contacts in Vibrational Energy Flow in Proteins. *J. Phys. Chem. Lett.* **2016**, *7*, 1950−1954.
(27) Yamashita, S.; Mizuno, M.; Tran, D.; Dokainish, H.; Kitao, A.; Mizutani, Y. Vibrational Energy Transfer from Heme through Atomic Contacts in Proteins. *J. Phys. Chem. B* **2018**, *122*, 5877−5884.
(28) Poudel, H.; Reid, K.; Yamato, T.; Leitner, D. Energy Transfer across Nonpolar and Polar Contacts in Proteins: Role of Contact fluctuations. *J. Phys. Chem. B* **2020**, *124*, 9852−9861.
(29) Yamashita, S.; Mizuno, M.; Mizutani, Y. High suitability of tryptophan residues as a spectroscopic thermometer for local temperature in proteins under non equilibrium conditions. *J. Chem. Phys.* **2022**, *156*, No. 075101.
(30) Mizuno, M.; Mizutani, Y. Role of atomic contacts in vibrational energy transfer in myoglobin. *Biophys. Rev.* **2020**, *12*, 511−518.
(31) Konkoli, Z.; Cremer, D. A New Way of Analyzing Vibrational Spectra. I. Derivation of Adiabatic Internal Modes. *Int. J. Quantum Chem.* **1998**, *67*, 1−9.
(32) Konkoli, Z.; Larsson, J. A.; Cremer, D. A New Way of Analyzing Vibrational Spectra. II. Comparison of Internal Mode Frequencies. *Int. J. Quantum Chem.* **1998**, *67*, 11−27.
(33) Konkoli, Z.; Cremer, D. A New Way of Analyzing Vibrational Spectra. III. Characterization of Normal Vibrational Modes in terms of Internal Vibrational Modes. *Int. J. Quantum Chem.* **1998**, *67*, 29−40.
(34) Konkoli, Z.; Larsson, J. A.; Cremer, D. A New Way of Analyzing Vibrational Spectra. IV. Application and Testing of Adiabatic Modes within the Concept of the Characterization of Normal Modes. *Int. J. Quantum Chem.* **1998**, *67*, 41−55.
(35) Kraka, E.; Zou, W.; Tao, Y. Decoding Chemical Information from Vibrational Spectroscopy Data: Local Vibrational Mode Theory. *WIREs: Comput. Mol. Sci.* **2020**, *10*, 1480.
(36) Kraka, E.; Quintano, M.; Force, H. W. L.; Antonio, J. J.; Freindorf, M. The Local Vibrational Mode Theory and Its Place in the Vibrational Spectroscopy Arena. *J. Phys. Chem. A* **2022**, *126*, 8781−8900.
(37) Wilson, E. B.; Decius, J. C.; Cross, P. C. *Molecular Vibrations: The Theory of Infrared and Raman Vibrational Spectra*; McGraw-Hill, New York, 1955.
(38) Woodward, L. A. *Introduction to the Theory of Molecular Vibrations and Vibrational Spectroscopy*; Oxford University Press, Oxford, 1972.
(39) Herzberg, G. *Molecular Spectra and Molecular Structure. Volume II: Infrared and Raman Spectra of Polyatomic Molecules*; Krieger Publishing Co, New York, 1991.
(40) Herzberg, G.; Huber, K. P. *Molecular Spectra and Molecular Structure; IV. Constants of Diatomic Molecules*; Van Nostrand, Reinhold: New York, 1979.
(41) Califano, S. *Vibrational States*; Wiley, New York, 1976.
(42) Zou, W.; Izotov, D.; Cremer, D. New Way of Describing Static and Dynamic Deformations of the Jahn-Teller Type in Ring Molecules. *J. Phys. Chem. A* **2011**, *115*, 8731−8742.
(43) Zou, W.; Filatov, M.; Cremer, D. Bond Pseudorotation, Jahn-Teller, and Pseudo-Jahn-Teller Effects in the Cyclopentadienyl Cation and its Pentahalogeno Derivatives. *Int. J. Quantum Chem.* **2012**, *112*, 3277−3288.
(44) Zou, W.; Cremer, D. Description of Bond Pseudorotation, Bond Pseudolibration, and Ring Pseudoinversion Processes Caused by the Pseudo-Jahn-Teller Effect: Fluoro Derivatives of the Cyclopropane Radical Cation. *Aust. J. Chem.* **2014**, *67*, 435.
(45) Cremer, D.; Pople, J. A. General Definition of Ring Puckering Coordinates. *J. Am. Chem. Soc.* **1975**, *97*, 1354−1358.
(46) Frisch, M. J.; Trucks, G. W.; Schlegel, H. B.; Scuseria, G. E.; Robb, M. A.; Cheeseman, J. R.; Scalmani, G.; Barone, V.; Petersson, G. A.; Nakatsuji, H.; Li, X.; Caricato, M.; Marenich, A. V.; Bloino, J.; Janesko, B. G.; Gomperts, R.; Mennucci, B.; Hratchian, H. P.; Ortiz, J. V.; Izmaylov, A. F.; Sonnenberg, J. L.; Williams-Young, D.; Ding, F.; Lipparini, F.; Egidi, F.; Goings, J.; Peng, B.; Petrone, A.; Henderson, T.; Ranasinghe, D.; Zakrzewski, V. G.; Gao, J.; Rega, N.; Zheng, G.; Liang, W.; Hada, M.; Ehara, M.; Toyota, K.; Fukuda, R.; Hasegawa, J.; Ishida, M.; Nakajima, T.; Honda, Y.; Kitao, O.; Nakai, H.; Vreven, T.; Throssell, K.; Montgomery, J. A., Jr.; Peralta, J. E.; Ogliaro, F.; Bearpark, M. J.; Heyd, J. J.; Brothers, E. N.; Kudin, K. N.; Staroverov, V. N.; Keith, T. A.; Kobayashi, R.; Normand, J.; Raghavachari, K.; Rendell, A. P.; Burant, J. C.; Iyengar, S. S.; Tomasi, J.; Cossi, M.; Millam, J. M.; Klene, M.; Adamo, C.; Cammi, R.; Ochterski, J. W.; Martin, R. L.; Morokuma, K.; Farkas, O.; Foresman, J. B.; Fox, D. J.. *Gaussiañ16 Revision B.01*; Gaussian Inc: Wallingford CT, 2016.
(47) Wilson, E. B. Some Mathematical Methods for the Study of Molecular Vibrations. *J. Chem. Phys.* **1941**, *9*, 76−84.
(48) Cremer, D.; Larsson, J. A.; Kraka, E. New Developments in the Analysis of Vibrational Spectra on the Use of Adiabatic Internal Vibrational Modes. In *Theoretical and Computational Chemistry*, Parkanyi, C., Ed.; Elsevier: Amsterdam, 1998; pp 259−327.
(49) Zou, W.; Kalescky, R.; Kraka, E.; Cremer, D. Relating Normal Vibrational Modes to Local Vibrational Modes with the Help of an Adiabatic Connection Scheme. *J. Chem. Phys.* **2012**, *137*, No. 084114.
(50) Yannacone, S.; Freindorf, M.; Tao, Y.; Zou, W.; Kraka, E. Local Vibrational Mode Analysis of π-Hole Interactions between Aryl Donors and Small Molecule Acceptors. *Crystals* **2020**, *10*, 556.
(51) Zou, W.; Freindorf, M.; Oliveira, V.; Tao, Y.; Kraka, E. Weak and strong π interactions between two monomers − assessed with local vibrational mode theory 2023, DOI: 10.1139/cjc-2022-0254.
(52) Sodupe, M.; Lluch, J.; Olivia, A.; Illas, F.; Rubio, J. *Ab initio* study of the ground and low-lying states of FeH. *J. Chem. Phys.* **1990**, *92*, 2478−2480.
(53) Bauschlicher, C. W.; Langhoff, S. Theoretical confirmation of a $^4\delta$ ground state for FeH. *Chem. Phys. Lett.* **1988**, *145*, 205−210.
(54) Hendrickx, M. F. A.; Anam, K. A New Proposal for the Ground State of the FeO^- Cluster in the Gas Phase and for the Assignment of Its Photoelectron Spectra. *J. Phys. Chem. A* **2009**, *113*, 8746−8753.
(55) Bagus, P. S.; Preston, H. Lowest $^5\Sigma^+$ state of FeO: An *ab initio* investigation. *J. Chem. Phys.* **1973**, *59*, 2986−3002.
(56) Mayer, I. Charge, bond order and valence in the AB initio SCF theory. *Chem. Phys. Lett.* **1983**, *97*, 270−274.
(57) Mayer, I. On bond order and valence in the Ab initio quantum chemical theory. *Int. J. Quantum Chem.* **1986**, *29*, 73−84.
(58) Mayer, I. Bond order and valence indices: A personal account. *J. Comput. Chem.* **2007**, *28*, 204−221.
(59) Cremer, D.; Kraka, E. Chemical Bonds without Bonding Electron Density? Does the Difference Electron-Density Analysis Suffice for a Description of the Chemical Bond? *Angew. Chem., Int. Ed.* **1984**, *23*, 627−628.
(60) Cremer, D.; Kraka, E. A Description of the Chemical Bond in Terms of Local Properties of Electron Density and Energy. *Croatica Chem. Acta* **1984**, *57*, 1259−1281.
(61) Kachalova, G. S.; Popov, A.; Bartunik, H. A Steric Mechanism for Inhibition of CO Binding to Heme Proteins. *Science* **1999**, *284*, 473−476.
(62) Watanabe, Y.; Nakajima, H.; Ueno, T. Reactivites of Oxo and Peroxo Intermediates Studied by Hemoprotein Mutants. *Acc. Chem. Res.* **2007**, *40*, 554−562.

https://doi.org/10.1021/acs.biochem.3c00192
Biochemistry XXXX, XXX, XXX−XXX

(63) Olson, J.; Soman, J.; Phillips, G., Jr Ligand pathways in myoglobin: A review on trp cavity mutations. *IUBMB Life* **2007**, *59*, 552−562.
(64) Liong, E.; Dou, Y.; Scott, E.; Olson, J.; Phillips, G., Jr Waterproofing the Heme Pocket. Role of Proximal Amino Acid Side Chains in Preventing Hemin Loss From Myoglobin. *J. Biol. Chem.* **2001**, *276*, 9093−9100.
(65) Samuel, P. P.; Case, D. Atomistic Simulations of Heme Dissociation Pathways in Human Methemoglobins Reveal Hidden Intermediates. *Biochemistry* **2020**, *59*, 4093−4107.
(66) Maier, J. A.; Martinez, C.; Kasavajhala, K.; Wickstrom, L.; Hauser, K. E.; Simmerling, C. ff14SB: Improving the Accuracy of Protein Side Chain and Backbone Parameters from ff99SB. *J. Chem. Theory Comput.* **2015**, *11*, 3696−3713.
(67) Case, D.; Ben-Shalom, I.; Brozell, S.; Cerutti, D.; Cheatham, T.; Cruzeiro, V.; Darden, T.; Duke, R.; Gohoreishi, D.; Gilson, M.; H, G.; Goetz, A.; Greene, D.; Harris, R.; Homeyer, N.; Izadi, S.; Kovalenko, A.; Kurtzman, T.; Lee, T.; LeGrand, S.; Li, P.; Lin, C.; Liu, J.; Luchko, T.; Luo, R.; Mermelstein, D.; Merz, K.; Miao, Y.; Monard, G.; Nguyen, C.; Nguyen, H.; I, O.; Onufriev, K.; Pan, F.; Qi, r.; Roe, D.; Roitberg, A.; Sagui, C.; Schott-Verdugo, S.; Shen, J.; Simmerling, C.; Smith, J.; Salomon-Ferrer, R.; Swails, J.; Walker, R.; Wang, J.; Wei, H.; Wolf, R.; Wu, X.; Xiao, L.; York, D.; Kollman, P. *AMBER*; University of California, San Francisco, 2018.
(68) Chai, J.-D.; Head-Gordon, M. Long-range corrected hybrid density functionals with damped atom-atom dispersion corrections. *Phys. Chem. Chem. Phys.* **2008**, *10*, 6615−6620.
(69) Ditchfield, R.; Hehre, W.; Pople, J. Self-consistent Molecular-Orbital Methods. IX. An Extended Gaussian-Type Basis for Molecular-Orbital Studies of Organic Molecules. *J. Chem. Phys.* **1971**, *54*, 724−728.
(70) Hariharan, P. C.; Pople, J. The influence of polarization functions on molecular orbital hydrogenation energies. *Theo. Chim. Acta* **1973**, *28*, 213−222.
(71) Chung, L. W.; Sameera, W.M.C.; Ramozzi, R.; Page, A.; Hatanaka, M.; Petrova, G.; Harris, T.; Li, X.; Z, K.; F, L.; Li, H.; Ding, L.; Morokuma, K. The ONIOM Method and Its Applications. *Chem. Rev.* **2015**, *115*, 5679−5796.
(72) Della Longa, S.; Pin, S.; Cortès, R.; Soldatov, A.; Alpert, B. Fe-Heme Conformations in Ferric Myoglobin. *Biophys. J.* **1998**, *75*, 3154−3162.
(73) Zou, W.; Tao, Y.; Freindorf, M.; Makoś, M. Z.; Verma, N.; Cremer, D.; Kraka, E. *Local Vibrational Mode Analysis (LModeA. Computational and Theoretical Chemistry Group (CATCO)*; Southern Methodist University: Dallas, TX, USA, 2022.
(74) Reed, A. E.; Curtiss, L.; Weinhold, F. Intermolecular interactions from a natural bond orbital, donor-acceptor viewpoint. *Chem. Rev.* **1988**, *88*, 899−926.
(75) Weinhold, F.; Landis, C. *Valency and Bonding: A Natural Bond Orbital Donor-Acceptor Perspective*; Cambridge University Press: Cambridge, UK, 2005.
(76) Keith, T.. *AIMALL*; TK Gristmill Software: Overland Park, KS, 2017.
(77) Kraka, E.; Larsson, J. A.; Cremer, D. Generalization of the Badger Rule Based on the Use of Adiabatic Vibrational Modes. In *Computational Spectroscopy*, Grunenberg, J., Ed.; Wiley: New York, 2010; pp 105−149.
(78) Bader, R. F. W. A quantum theory of molecular structure and its applications. *Chem. Rev.* **1991**, *91*, 893−928.
(79) Kraka, E.; Setiawan, D.; Cremer, D. Re-Evaluation of the Bond Length-Bond Strength Rule: The Stronger Bond Is not Always the Shorter Bond. *J. Comput. Chem.* **2016**, *37*, 130−142.
(80) Kraka, E.; Cremer, D. Weaker Bonds with Shorter Bond Lengths. *Rev. Proc. Quim.* **2012**, *6*, 31−34.
(81) Chakrabarti, P.; Bhattacharyya, R. Geometry of nonbonded interactions involving planar groups in proteins. *Prog. Biophys. Mol. Biol.* **2007**, *95*, 83−137.

https://doi.org/10.1021/acs.biochem.3c00192
Biochemistry XXXX, XXX, XXX−XXX